SAND2022-1211J

Evaluation of Applied Stress on Atmospheric Corrosion and Pitting Characteristics in 304L Stainless Steel

John B. Plumley,,** Christopher L. Alexander,*** Xin Wu,**** Scott Gordon,***** Zhenzhen Yu,***** Nicholas Kemp,* Fernando H. Garzon,*,** Eric J. Schindelholz,****** and Rebecca F. Schaller‡,**

‡Corresponding author. E-mail: rschall@sandia.gov.

*Materials Science and Engineering, Sandia National Laboratories, Albuquerque, New Mexico 87185, USA.

**Center for MicroEngineered Materials, University of New Mexico, Albuquerque, NM 87106.

****Department of Civil & Environmental Engineering, University of South Florida, 4202 E. Fowler Avenue, Tampa, FL 33620-5359.*

****School of Chemical Engineering and Technology, Sun Yat-Sen University, Zhuhai, 519082, China.

*****Center for Welding, Joining, & Coatings Research, Department of Metallurgical and Materials Engineering, Colorado School of Mines, Golden, CO 80401.

******Department of Materials Science and Engineering, The Ohio State University, Columbus, OH 43210

ABSTRACT

The effects of applied stress, ranging from tensile to compressive, on the atmospheric pitting corrosion behavior of 304L stainless steel (SS304L) were analyzed through accelerated atmospheric laboratory exposures and microelectrochemical cell analysis. After exposing the lateral surface of a SS304L four-point bend specimen to equivalent relative humidity seawater at 50 °C and 35 % RH for 50 days, pitting characteristics were determined using optical profilometry and scanning electron microscopy (SEM). The SS304L microstructure was analyzed using electron backscatter diffraction (EBSD). Additionally, localized electrochemical measurements were carried out on a similar, unexposed, SS304L four-point bend bar to determine the effects of applied stress on corrosion susceptibility. Under the applied loads and the environment tested, the observed pitting characteristics showed no correlation with the applied stress (from 250 to -250 MPa). Pitting depth, surface area, roundness, and distribution were found to be independent of location on the sample or applied stress. The lack of correlation between pitting statistics and applied stress was more likely due to the aggressive exposure environment, with a sea salt loading of 4 g/m^2 chloride. The pitting characteristics observed were instead governed by the available cathode current and salt distribution, which are a function of sea salt loading, as well as pre-existing underlying microstructure. In microelectrochemical cell experiments carried out in Cl^- environments comparable to the atmospheric exposure and in environments containing orders of magnitude lower Cl^- concentrations, effects of the applied stress on corrosion susceptibility were only apparent in open circuit potential in low Cl^- concentration solutions. Cl^- concentration governed the current density and transpassive dissolution potential.

KEY WORDS: *Localized Corrosion, Marine Environments, and Electrochemical Microcell*

1 Introduction

Austenitic stainless steel is commonly used in marine environments due to its high resistance to corrosion.[1] One example of its use is in the construction of spent nuclear fuel (SNF) interim storage canisters. However, in a chloride containing atmosphere, such as in marine or near marine conditions, where airborne particulates can absorb and deliquesce on metal surfaces, localized corrosion in the form of pitting is of great issue.[2-4] Pitting corrosion on stainless steel is due to the localized breakdown of the passive oxide film, which can be caused by temperature,[5] roughness,[6] mechanical stress,[7] electrochemical breakdown,[8] changes in pH,[9] breakdown by chloride ions,[10] and MnS inclusions.[11] Pitting can lead to stress corrosion cracking (SCC),[12] which has been observed to initiate from pits and can occur in corrosive environments when a significant tensile stress is present.[13-18] Additionally, strain and applied tensile stress has been observed to increase corrosion susceptibility,[19, 20] enhance pitting initiation and propagation,[21-24] and ultimately lead to cracking in stainless steel alloys.[25-32] It is critically important to fully understand the influence that applied stress has on pit morphology, pit size, and pit distribution under atmospheric exposure to better determine the potential severity for pit to crack initiation and SCC under relevant atmospheric environments for SNF canisters.[33]

SCC is of specific concern for SNF storage canisters when the following conditions required for SCC occur: a corrosive environment (brines can form from chloride containing dust deposition in marine locations[4]), a susceptible material (in the case of SNF storage canisters, austenitic stainless steel,) and significant residual stresses (formed from welding during canister manufacture).[34-37] Even under these conditions, it is still a challenge to predict the location, timing, and severity for the initiation of SCC on SNF canister. There have been numerous studies on accelerated atmospheric exposures of pitting,[3, 33, 38-48] yet many questions remain regarding how stress affects pitting, the answers to which will provide valuable information for further understanding pit-to-crack transition behavior.

Pitting corrosion is a concern in stainless steel because it has been correlated in many cases with crack initiation.[2, 16-18, 33, 49-53] For example, Weirich et al. found microcracks associated with pits; about 1/3 of pits formed in 304 stainless steel (SS304) atmospherically exposed coupons printed with artificial seawater and exposed for one year at 40 % relative humidity (RH) were associated with microcracks.[2] The tensile stress required for microcracking was believed to be due to the initial polishing treatment of the stainless steel samples, as the study by Weirich et al. did not implement externally applied stress.[2] In the case of an applied stress on 316L stainless steel (SS316L) under 0.1 % elastic load and atmospherically exposed for 6 months under $MgCl_2$ and $MgCl_2$:$FeCl_3$ droplets at 50 °C and 30 % RH, Ornek[33] observed SCC with two types of crack morphologies being dependent on distance to the pit mouth. Specifically, cracks located at the edge of the pit mouth tended to be smaller and propagated in a zigzag-like pattern; while at a distance of ~ 10 µm from the pit mouth, cracks exhibited a larger width-to-length ratio.[33] In another study of SS304 four-point bend specimens deposited with $MgCl_2$, atmospherically exposed at 60 °C and 45 % RH, Turnbull et al. observed that each crack had an associated pit, with small cracks extending from the pit mouth, larger cracks at the pit base, and multiple pits along crack lengths.[17] Turnbull et al. also evaluated how externally applied stress can affect the location of maximum stress in and around pits using finite element analysis (FEA).[16, 18] More importantly,

it was shown that in the case of a growing pit, a static stress field can lead to a local dynamic plastic strain that is significant to the susceptibility of SCC.[16] As cracks have been shown to be associated with pits, it is beneficial to focus on understanding how pitting properties relate to cracking, specifically under applied stress.

Pit size and density are parameters that have been shown to correlate with cracking.[49, 51, 54] Larger pits are more likely to evolve into cracks,[49, 54] and regions of higher pitting density initiate cracks that are more likely to lead to material failure.[54] The Kondo criteria predicts that pitting can evolve into cracking when pit depth is greater than a specific threshold, or critical depth in low alloy steel.[49] For martensitic stainless steel, McMurtrey et al. experimentally observed that cracking correlated with pit depth and density, in that cracks that led to fractures of the testing coupons initiated from pits with depths and local densities in the higher percentile, generally >97.5 percentile.[54] However, cracks did not initiate at the deepest pits, nor did cracking initiate in the region of highest pit density for samples pre-corroded in a fog chamber of 0.9 M NaCl electrolyte and subsequently fatigued. In one example, the crack initiating pit that led to fracture was ~ 70 µm deep (which was greater than 97.5% of pits on the coupon) with the deepest pit on the coupon being ~ 110 µm.[54] Further study is necessary to validate modeling and theoretical assumptions of the relationships between pit size/density and pit to crack initiation.

Pit morphology may also play a large role in SCC susceptibility. Irregular (non-hemispherical) pit morphologies have exhibited features that may serve as stress concentrators, thus increasing the chance for pit to crack transition.[16] For instance, microstructural attack can yield more complex pit morphologies with sharp features with high aspect ratios.[2, 55] High depth-to-width aspect ratio features have been shown through modeling to heavily affect the location and magnitude of stress concentration.[51, 56] Cerit et al. found through FEA that elastic stress concentration factor increases overall with pit aspect ratio, with concentrated stress being the most pronounced at the bottom of more wide-shallow (low aspect ratio) pits where secondary pitting and cracking is most likely to occur.[56] Mai et al. utilized phase-field modelling to observe that cracks initiate at the points of highest curvature within a pit where localized stress concentration is highest.[51] In 304 stainless steel, Weirich et al. showed that more irregular pits with microstructural attack contain cracks originating from inside pits during atmospheric corrosion at 40% RH, as opposed to more smooth hemispherical pits that were observed at 76% RH, where no cracks were observed.[2] However, it was not definitively determined that the sharp fissure-like features revealed from the microstructural attack was the actual cause of cracking. Co and Burns found that for intergranular corrosion morphology in aluminum alloy, cracks were correlated from planes with higher fissure depth and densities.[57] There is a probable link between irregular pitting and cracking due to a higher degree of localized stress concentrators, but the influence of applied stress on pit morphology is unknown.

Externally applied stress has been shown to enhance the pitting properties that can lead to cracking and ultimate failure.[30, 58-60] Under full immersion, applied stress has been found to increase anodic dissolution in stainless steel during pitting,[58, 59] which in turn could lead to larger pits because it enhances stable pit growth.[60] Applied stress can also accelerate pit initiation,[30] potentially yielding a higher density of pits in regions of higher stress. Suter et al. found that applied stress causes cracking in MnS inclusions, which results in active pitting.[21] It is unclear what effects applied stress has on the resultant pit morphology; however, pit morphology is significant to SCC, as pit irregularities or asperities may act as significant stress concentrators. Wu and Singh found that applied elastic stress had no effect on the size and morphology of pits in 304SS under full immersion experiments, despite a notable

decrease in pitting potential.[24] However, applied stress can change the location of concentrated stress points within a pit.[16] For instance, Turnbull et al. showed that with applied elastic strain, stress is maximized at the pit shoulder, whereas stress redistributes to the pit base under inelastic strain.[16] There could be additional interplay or effects of pit morphology on subsequent pit growth due to heterogeneously concentrated stresses. Considering the potential effect applied stress could have on pit morphology, experimental evidence is important to obtain a better understand of how changes in morphology from stress in a growing pit can increase the risk of cracking.

Under canister relevant conditions, during atmospheric corrosion, it is still of interest to evaluate the relevance of stress as a deleterious factor and how it governs pitting in comparison to environmental factors, such as RH and Cl^- concentration, and underlying microstructure. Further understanding the effects of externally applied or residual stress under low RH conditions, which result in irregular pitting and higher degree of localized stress concentrators is necessary to fully understand the risks of SCC.

The goal of this study is an attempt to probe, using a large set of data, the dependence of pit morphology, pit size, and pit distribution on applied stress under environmental exposure conditions pertinent to a SNF canister. A probable condition was selected for exposures; 50 °C and 35 % RH, where deliquescence of bischofite, $MgCl_2$, occurs but not halite, NaCl[61] (resulting in a $MgCl_2$ rich brine surrounding solid NaCl crystals). A high deposition of artificial seawater with a Cl^- loading density of 4 g/m^2 is used to accelerate corrosion conditions. The study presented herein provides a large data set analyzing the size and morphology of pits and crevice corrosion features, over 14,000 points produced across a full range of tensile and compressive stresses, 250 to -250 MPa (a stress range comparable to weld residual stresses present in SNF canisters), on the same surface of an exposed SS304L four-point bend bar. The resultant pit distribution, size, and morphology with respect to the three different stress regions—tensile, minimally stressed, and compressive—were determined through optical profilometry (OP) and scanning electron microscopy (SEM). To compliment the findings of the atmospheric exposure results, locally obtained electrochemical parameters versus the range of applied stress, breakdown potential (E_B), open circuit potential (OCP), and current density (*i*), were obtained through microelectrochemical cell measurements in aggressive and benign surrogate chloride solutions.

2 Experimental Procedures

2.1 Materials and Sample Preparation

2.2.1 SS304L Sample Preparation

The base steel was processed by the manufacturer North American Stainless in an electrical arc furnace (EAF), refined through argon oxygen decarburization (AOD), and further processed with continuous casting. Two, 320 mm long, 16.5 mm wide, and 15.9 mm thick SS304L samples (composition provided in Table 1) were cut out along the transverse direction from the base metal plate. One cut sample was prepared for atmospheric exposure and the second for electrochemical experiments. The exposed surface was mechanically polished to 0.1 Ra µm mirror-like finish.[62]

2.1.2 Applied Stress and Stress Distribution Profiles

Four-point bend apparatuses were used to replicate the residual stresses present in SNF canisters. These were designed according to ASTM D6272-10,[63] and painted with Kolor-Proxy high build polyamide-epoxy primer to provide abrasion and corrosion resistance, see photograph in Figure 1b. The

SS304L bars were placed under a displacement load using two screws in the four-point bend apparatus as seen in Figure 1a. Finite element analyses (FEA) modelling was used to determine the loading frame and sample geometry that would result in the levels of strain needed for the desired stress load.[62] While ASTM G39[64] can be applied for calculating the stress along the top surface of the four-point bend bar, FEA analysis was necessary here to determine the stress gradient along the full front face. Stress distribution from FEA is displayed in Figure 1c. Digital image correlation (DIC) was implemented in order to load the bar to the actual strain level. For DIC, strain evolution was monitored along the X-axis during sample loading as a function of Y-displacement. A low-chloride black paint was applied to the three unexposed surfaces and ends of the SS304L bar in a speckle pattern, to allow for DIC. DIC was performed on the speckle pattern coated side of the four-point bend bar, rather than the opposite uncoated atmospherically exposed side. As the speckle pattern was applied to the unexposed side, and not the region of interest, it was not removed from the bar for the atmospheric exposure. DIC tracks changes in the features of the speckle pattern (which deforms with the sample) to correlate displacements from the reference state. The two screws were turned to apply incremental Y-displacement loads while induced strain was monitored by DIC (Figure 1c) to achieve a stress level of 250 MPa (yield strength of SS304L is 250 MPa)[62] at the tensile face (matching the stress conditions of the heat affected zones of canister welds, regions of residual stress from welding where SCC is likely to occur).[62] The measured DIC was compared to the predicted stresses from FEA and displayed good agreement, Figure 1c and Figure 1d.[62]

2.1.3 Brine Deposition and Atmospheric Exposure

One SS304L bar, loaded in the four-point bend apparatus, was preheated to 50 °C for 30 minutes in a drying chamber with 0 % relative humidity (RH). It was then placed in a deposition chamber, where artificial seawater (ASW) (prepared according to ASTM D1141)[65] was applied as a mist using a humidifier nozzle. The deposition composition was prepared to the composition given in Table 2 for ASTM ASW at 25 °C [66,67]. The bar was taken out every five minutes, dried for three minutes in the drying chamber, and imaged as incremental amounts of salt were deposited. In order to monitor the amount of salt being deposited on the four-point bend sample, six test coupons (5 x 5 cm^2) were placed in the deposition chamber concurrently. One coupon was removed every 10 min, the deposited salt was dissolved in 250 mL DI water, and the chloride ion concentration determined through conductivity measurements. This cycle was repeated until an ASW loading density of 4 g/m^2 chloride was achieved.[62] This high chloride deposition density was selected to accelerate corrosion rates. The stressed, salt-loaded, SS304L bar was then placed in a humidity chamber and exposed for 50 days at conditions pertinent to SNF canister environment, 50 °C and 35 % RH.

2.1.4 Cleaning Procedure

Following exposure, in order to remove excess salts and corrosion product, the stressed, corroded SS304L bar was cleaned by submersion in 0.6 M diammonium citrate solution at 70 °C for 24 hours (ASTM-G1).[66] The corroded surface was then brushed with a soft brush in the diammonium citrate solution and rinsed with deionized (DI) water. The sample surface was then dried with nitrogen.

2.2 Post-Mortem Surface Characterization

2.2.1 Ferrite Analysis with Feritscope

Ferrite volume fraction was measured via magnetic induction by using a FMP30 Feritscope, from FischerTechnology, (detection range 0.1 to 80 vol%) over the mirror polished surfaces of the two SS304L samples. The amount of ferrite in the samples was below the detectable limits of the feritscope.

2.2.2 Scanning Electron Microscopy

SEM analysis was carried out to examine corrosion damage and observe pitting morphology across the atmospherically exposed and cleaned bar. Micrographs were taken with a Zeiss Supra 55-VP field emission SEM operated at 15 kV and a working distance of 10 mm.

2.2.3 Electron Backscatter Diffraction

Electron backscatter diffraction (EBSD) was performed on a cross section of the exposed four-point bend bar using the Zeiss Supra 55-VP SEM equipped with a symmetry EBSD detector. An accelerating voltage of 15 kV was used with a 50 nm step size. Cross sections were obtained perpendicular to the applied stress field of the atmospherically exposed four-point bend bar to evaluate the entire applied stress range, as well as the near surface region (The cross section of the sample that EBSD was performed on is indicated by the dotted yellow line in Figure 3). Prior to EBSD, samples were polished with two final vibratory polishing steps, first in a 0.3 μm Al_2O_3 slurry followed by a 0.04 μm SiO_2 slurry for 24 hours each.

2.2.4 Optical Profilometry

A ZYGO Nexview NX2 3D Optical Profilometer was used to profile the surface of the atmospherically exposed and cleaned bar to statistically analyze pit morphology and distribution between the stressed regions. A total surface area of 145 mm by 13 mm was scanned at 5.5X magnification, with 1X zoom, and 2.3 % light level. This was performed by combining five 29 by 13 mm scans; see Figure 3 for an example of a 29 mm by 13 mm scan and the respective stressed regions of interest. To achieve the full area scan, sub-scans of 1.25 mm by 1.25 mm were cumulatively stitched with a 10 % overlap. This area was selected to record the corrosion damage that occurred over the stressed regions across the maximal stressed length of the bar, along the L_2 path in Figure 1d.

2.2.5 Image Processing and Statistical Analysis

The images obtained from 3D profilometry were processed using MountainsMap version 7.4 Imaging Topography software. Depth and area information was collected for statistical analysis. For comparison, the data was grouped according to the labels “tensile”, “minimally stressed”, and “compressive” regions which were extracted in 3 mm height rectangles based on the stress profile in Figure 2a determined from FEA and are shown in Figure 3. The criteria for defining a pit was any hollow indentation in the surface of the SS304L bar that was > 10^{-6} mm^2 in area and > 10^{-5} μm in depth. These sizes are within the profilometer resolution, which is $3.7x10^{-6}$ mm^2 laterally for the 5.5X objective lens used and $6x10^{-5}$ μm in the Z direction. Any detected motifs smaller than 10^{-5} mm^2 show up as a small collection of pixels on the image analysis software and were therefore rejected as artifacts. To remove additional artifacts, such as polishing scratches and surface roughness, from the profilometry measurements, the image threshold was set to 8 % of the image’s original light intensity, where points in the image outside of the threshold, including scratches from polishing, were set as non-measured points, subsequently generating a new

topographic image without scratches and roughness artifacts. This threshold removal resulted in pit depth on average being 0.11 % smaller and a reduction of pit area on average of 17.6 %. This larger area reduction is due to the loss of both shallow artifacts and scratches as well as some shallow pit regions in which the light intensity in the image is lowered. To better account for the software identifying multiple motifs within the same pit, a smoothing filter was used that merged identified pits less than 20 µm in depth and 2.0 x 10^{-4} mm^2 in area with neighboring pits. Pits that meet the pruning criteria that could not be merged with neighboring pits were still included in the analysis. The pit depth, area, and roundness were extracted, and the cumulative distribution was plotted comparing the distribution of the parameters between the tensile, minimally stressed, and compressive regions. Roundness, as measured here, is defined as the area of the pit divided by the area of a circle, derived from the maximum diameter of the pit:

$$roundness = \frac{4Area}{\pi D_{max}^2} \quad (1)$$

Where *Area* refers to the area of the pit, and D_{max} is the maximum diameter of the pit. The closer the *roundness* value is to one, the more circular the pit.[67]

Using OriginPro graphing and data analysis software, Kolmogorov-Smirnov Tests (KS-Tests) with α=0.05[68] were applied to quantitatively analyze any significant differences in parameter distribution.

For an understanding of how pit morphology might relate to pit size, the roundness versus pit depth and pit area were compared through Pearson's r Correlation Coefficient test. This test is a quantitative determination of the relationship strength between two random variables X and Y by using the equation:

$$\rho_{x,y} = \frac{cov(X,Y)}{\sigma_x \sigma_y} = \frac{E((X - E(X))(Y - E(Y)))}{\sigma_x \sigma_y} \quad (2)$$

Where σ_x and σ_y are standard deviations of X and Y variables, *cov(X,Y)* = covariance, and *E(.)* is the expected variable value.[69]

2.3 Microelectrochemical Scans

Local, spatially selective electrochemical investigations were carried out using a microelectrochemical setup with a Gamry Reference 600+ potentiostat and a Warner Instruments triple electrode holder with a capillary opening. The capillary had an outer diameter of 1.0 mm with an inner diameter of 0.58 mm. A silicone paste, DOW CORNING® 3140 MIL-A-46146 RTV COATING hydroxyl terminated, non-corrosive, flowable, room temperature curing silicone rubber was applied to create a seal at the electrolyte-metal surface interface. This paste was heated to 150 °C for 1 hour to partially remove surface hydroxyl groups resulting in a more hydrophobic silicone surface, preventing aqueous electrolyte from seeping under the seal during measurement. The applied silicone paste resulted in an average surface area on the SS304L working electrode 0.089 mm^2, which was determined from optical imaging of the capillary opening with the silicone rubber applied. Optical images of exposed areas of the electrode surface were examined pre and post electrochemical testing to confirm the lack of crevice corrosion. After introduction of the additional heat treatment step of the silicone paste, no crevice corrosion was observed during testing. Salt electrolyte solutions of the following concentrations: 0.1 M NaCl, 1 M NaCl, 0.05 M $MgCl_2$, and 0.5 M $MgCl_2$ were prepared in DI water. The working electrode was the unexposed SS304L four-point bend bar, with a Pt wire counter electrode, and a Ag/AgCl wire reference electrode.[70] Prior to each

potentiodynamic scan, an OCP was established for 300 s. Potentiodynamic polarization was carried out at a scan rate of 1 mV/s from -0.1 V vs OCP to a final potential of 1.3 $V_{Ag/AgCl}$. Each scan was repeated 5 times at different locations within each constant maximum stress region for consistency. Figure 3 illustrates an example of how five measurements per stress region was taken for a single brine. Regions of constant tensile and compressive stress were determined from the FEA map shown in Figure 1d, which reveals separate constant tensile and compressive stress regions of about 150 mm by 2 mm each.

3 Results

Electron backscatter diffraction (EBSD) band contrast maps of a cross section taken through the center of the atmospherically exposed SS304L bar (Figure 4) post corrosion and after removal of the bar from the four-point bend apparatus are shown in Figure 5 (a). Inverse pole figure maps from the same cross section are shown in Figure 5 (b) and Figure 6 (a-c). No real difference between average grain size and shape could be discerned between the different stress regions from the band contrast and pole figure maps. Using ImageJ analysis software, average grain size was measured as 42 ± 4.4 μm in the tensile region, 43 ± 4.1 μm in the minimal stress region, and 41 ± 3.9 μm in the compressive region. These values are comparable to the typical SS304L grain size value of 40 μm.[71] Grains appear randomly distributed throughout the stress regions and are primarily equiaxed. There was no texture observed to be aligned with the applied stress regions. Additionally, Figures 5 (c) and inset, and Figure 6 (a-c) show the phase contrast maps of the sample cross section. The blue regions represent the secondary body centered cubic (BCC) phase, either martensite or delta ferrite, within the primary (red) austenite face centered cubic (FCC) phase. Using ImageJ, it was determined from the phase contrast maps in Figure 6 (a-c) that the percentage of the BCC phase distributed within the sample is 0.95 % in the tensile region, 2.90 % in the minimal stress region, and 1.60 % in the compressive stress region. The distribution of the secondary BCC phases within the primary austenite FCC phase does not seem to correlate to the different regions of applied stress.

Through SEM, four different prominent pit morphologies, visible in Figures 7 and 8, were observed across all stressed regions, with no apparent correlation to the applied stress. The four morphologies observed were categorized in Figure 8 as (a) hemispherical, (b) hemispherical with regions of selective microstructural attack, (c) a mix of crevice corrosion and irregular pitting, and (d) a mix of crevice corrosion and deep irregular pitting with regions of selective microstructural attack on slip bands. Microstructural attack is observed in the SEM as a crossed-hatch structure. Crevice corrosion can occur beneath the precipitated halite particles, where the moisture is confined, and corrosion promoters accumulate while the oxygen levels deplete.[40] This morphology is most obvious in Figures 8, (c) and (d), where the crevice corrosion damage appears more irregular and is shallow in attack depth.

The cumulative probability plots of pit depth, area, and roundness values measured through optical profilometry versus the defined stress regions are presented in Figure 9. Through visual inspection of the cumulative probability plots, no obvious differences are apparent between the measurements of pit depth, area, and roundness across each stress region. All cumulative distribution curves overlap, with the slight exception of the pit depth curve in the compressive region, the blue line in Figure 9a, which is lower than both the similar tensile and minimally stressed curves. When the KS-Test is applied between the compressive and tensile pit depth cumulative distribution curves, with an $\alpha = 0.05$ conventional

threshold parameter,[68, 72] a KS-statistic of 7.3% was calculated. This is a measure of how much the cumulative distribution of pit depths in the compressive region can deviate from that of the tensile region. However, as this was not consistent across the parameters measured, while this indicates a significant difference in pit depth, it is believed that applied stress does not play a dominant role with regards to pit size and shape.

From Pearson's r Correlation Coefficient test, the correlation coefficient between pit roundness and pit depth from the data sets (Figure 9a and Figure 9d) was determined to be 0.17, and for pit roundness and pit area (from Figure 9b and Figure 9d) was 0.049. As both correlation coefficients were determined to be "poor" (<0.2),[69] it was concluded that pit roundness was generally independent of pit size. Pit density was not clearly influenced by stress as there was no relation between pit density and the applied stress. Specifically, there were ~4456 detected pits in the tensile region (1024 pits/cm^2), ~5524 pits in the minimal stress region (1270 pits/cm^2), and ~4448 pits in the compressive region (1023 pits/cm^2). These pit densities are reasonably close to those reported previously obtained through similar profilometry analysis by Weirich et al.[2] yielded results of 961 pits/cm^2 for unstressed SS304L exposed for 1 year at 40 % RH, 35 °C, and loaded with 3 g/m^2 ASW. The similarity in pit density between the varied stress regions reported here and the unstressed steel by Weirich et al. further signifies that stress may not be responsible for the pit densities observed herein.

Representative microelectrochemical scans and corresponding open circuit potential (OCP) values measured for the pre-defined stress regions on the unexposed four-point bend bar are displayed in Figures 10 through 13. With the exception of a slight suppression in OCP in the tensile region for 0.1 M NaCl and 1.0 M NaCl solutions, no dependence on stress for OCP could reliably be observed for 0.1 M NaCl, 1.0 M NaCl, 0.05 M $MgCl_2$, and 0.5 M $MgCl_2$ solution concentrations as seen in Figures 10, 11, 12, and 13 (numerical OCP values are listed in Table 3). Across all solutions and concentrations, no breakdown potential (E_B) was observed. The regions on the potentiodynamic plots around 1 to 1.2 V vs. Ag/AgCl, where the anodic rate increases, is a result of transpassive dissolution[73] rather than E_B from corrosion of the SS304L. E_B of SS304 are reported to be between 190 and 295 mV vs Ag/AgCl by Suter et al.[21] Transpassive E_B values decrease from ~1.2 V for both NaCl solutions to about 1.1 V and 1 V for 0.05 M $MgCl_2$ and 0.5 M $MgCl_2$ solutions, respectively. From Table 3, it can be seen that current densities consistently measured at 0.8 V above OCV (taken from the region where current is least sensitive to change in potential) roughly double when the Cl^- concentration is increased by an order of magnitude, from 0.1 M to 1 M NaCl and 0.05 M to 0.5 M $MgCl_2$. The range of current densities observed in this study at the potentials scanned are consistent with literature.[74]

4 Discussion

Under the atmospheric conditions examined herein, the results displayed that pitting size, morphology, and distribution across the SS304L four-point bend bar were independent of applied tensile and compressive stress (the direction of applied stress relative to the evaluated surface is shown in Figure 1a). Instead, results from SEM, in Figures 7 and 8, and profilometry analysis, in Figure 9, indicate that the overall nature of the pitting process on the surface of the stressed bar, under the concentrated brine, is more highly dependent on the local environment established. Specifically, the electrolyte coverage and available cathodic current, which is dependent on electrolyte properties such as composition, conductivity, O_2 solubility, etc., govern the pitting process.[75, 76] The analysis of pitting characteristics revealed that various pit sizes, shapes, and densities over the sample occurred regardless of the pits'

position relative to the applied stress field. From SEM in Figures 7 and 8 it was observed that irregular shaped pits, hemispherical pits, pits with surrounding crevice corrosion, and pits with microstructural attack appear evenly distributed across the tensile, minimally stressed, and compressive regions. The results obtained from optical profilometry (Figure 9) indicate that pitting depth, area, and density also occur throughout all three stress regions without any statistical variance. The varied and limited available cathodic current, due to the electrolyte morphology and composition on the surface, is likely the main cause for the observance of microstructural attack and irregularities in pitting.

4.1 Stress Effects on Pit Morphology and Distribution

The inhomogeneous pitting response observed across the surface in this study is believed to be due, in part, to the cathodic current availability, in that the maximum pit size is governed by the anodic current demand and the available cathodic current.[75] However, the electrolyte coverage is non-homogenous and discontinuous, as is illustrated in Figure 14b. At the 35 % RH and 50 °C exposure conditions, solids (halite) precipitate out of the brine resulting in a discontinuous film of electrolyte.[61] In a modelling study by Katona et al., where pitting dynamics were analyzed in seawater with and without the consideration of salt precipitates, it is further supported that in the case of sea-water brine at 40% RH, cathode size was shown to be smaller and anodic demand higher when salt precipitates were considered.[77] The random, high-density salt distribution on the surface of the SS304L four-point bend bar observed in the SEM image from Figure 14a indicates that electrolyte coverage and geometry may differ greatly across the sample in a random manner.[78] As NaCl precipitates at the low RH examined herein, the composition of the electrolyte would be dominated by $MgCl_2$ (Table 2). The discontinuous brine, salt brine volume, and the random distribution and various sizes of the precipitated salt phases may affect the distribution of available cathodic current.

The possible cathode reactions in an aqueous environment include the oxygen reduction reaction (ORR) and hydrogen evolution reaction (HER):[76]However, it was demonstrated by Katona et al. that on SS304L, HER dominates in concentrated $MgCl_2$ solutions due to ORR suppression from formation of Mg-hydroxide.[76] This further suppresses the limited cathodic current, which could also contribute to the varied pitting sizes observed in this study. Given these limitations in cathodic current availability, meeting anodic current demand becomes more of an issue. Moreover, anodic current demand will increase as a result of applied stress, as stress has been observed to increase anodic dissolution.[58] The available cathodic current under these conditions is possibly insufficient to meet the enhanced anodic current demands due to the applied stress, and any potential effects of applied stress on pitting size are not observed. Therefore, the discontinuous brine coverage and the resulting limited cathodic current availability over the surface of the sample more likely govern the varied pitting size observed.

4.2 Electrolyte Coverage and Pit Morphology

The electrolyte coverage and available cathodic current not only play a role in pit size[75] but may also govern the development of pit morphology.[2] In regions where the cathodic current is limited (where smaller brine volumes are present), it cannot support the anodic demand for uniform corrosion of the varying microstructures, and as a result irregular pit growth with microstructural attack occurs. In other regions, which may have larger electrolyte volumes, and thus greater available cathodic current, hemispherical pit growth is supported. Both hemispherical pits as well as microstructurally etched and abnormally shaped pits were observed across the surface of the SS304L four-point bend bar. Additionally, crevice corrosion can occur beneath precipitated NaCl crystals and contribute to the

irregularity observed in pit morphologies.[78] An example of crevice corrosion vs. pitting can be seen in Figure 8d. From the EBSD results presented in Figures 5c and 6g-i, a body-centered-cubic (BCC) phase, likely martensite formed from cold working during material fabrication[79] or from polishing during sample preparation, was observed to be uniformly distributed throughout the sample. Therefore, the microstructural attack features observed are due to the combination of the random distribution of electrolyte and thus available cathodic currents and where this interacts with the pre-existing BCC phase (which is preferentially dissolved as compared to the parent austenitic face-centered-cubic (FCC) phase).[2, 41, 45, 46, 80] Stress induced martensite corrodes at a faster rate than austenite, i.e. preferential dissolution, due to higher dislocation density promoting corrosion.[81] Similar etched-like pit morphologies have been observed previously by Weirich et al.,[2] Mohammed-Ali et al.,[55] and Örnek et al..[46] In the study by Weirich, SS304L was exposed to sea salt particles for one year at 40 % RH at 35 °C, where the cross-hatched microstructural attack was attributed to preferential dissolution of slip bands. According to Mohammed-Ali et al.,[55] the BCC phases, similar to those observed in Figures 5 and 6, were either bands from ferrite, twinning, or strain induced martensite. They found that the cross-hatched features seen in the microstructural attack during pitting were austenite bands or rings, remaining due to the preferred dissolution of the BCC phase.[55] Therefore, the observed localized microstructural attack of the SS304L four-point bend bar is the result of more favorable-dissolution of a BCC secondary phase.[27, 55, 82] The applied stress was not high enough to induce martensite in the analyzed bar, as martensitic phase transformation in SS304L occurs more at lower temperatures (0 to 25 °C) and applied stress values significantly higher than 500 MPa,[83] and so applied stress effects are not observed to have an effect on pitting morphology. In summary, smooth hemispherical pits result in regions where there is sufficient cathode current to corrode both phases at the same rate, and pits with microstructural attack result in regions where there is insufficient cathode current and both phases corrode at different rates. The applied stress in this study does not seem to affect pit morphology, as smooth hemispherical pits and irregularly shaped pits with microstructural attack were observed regularly without any noticeable correlation to applied stress.

4.3 Effect of Stress on Electrochemical Parameters

In addition to limited cathodic current availability, it is believed that the aggressive, high chloride environment of the atmospheric exposure dominated pitting susceptibility and governed any effects produced by localized stresses. No effects of applied stress on pitting were observed on the salt loaded bar under the atmospheric exposure conditions of this study despite a full range of applied tensile to compressive stresses (-250 to +250 MPa, the yield strength of SS304 is about 250 MPa).[62] However, in the case of the microelectrochemical cell, where oxygen is more readily available, the increased anodic demands under conditions of applied stress are more likely to be met by the cathodic supply. This is assuming oxygen is not depleted at the cathode interface which would result in concentration polarization where the current becomes diffusion-limited. From past electrochemical studies, the major known effects of stress on corrosion of stainless steel are increased corrosion susceptibility, as shown by lower OCP found by Nazarov et al.[19] under plastic deformation and shown by Shi et al.[84] under elastic deformation (similar to the case studied here), lower breakdown potential (E_B) by Wu and Singh,[24] and an increase in passive current density (i_{pass}) by Navai.[85] Here, the Stress effects on *i* and transpassive E_B could still not be observed from localized measurements performed in the microelectrochemical cell, neither from the lower chloride concentrations (0.1M NaCl and 0.05M $MgCl_2$), nor under the more concentrated Cl^- solutions (1M NaCl and 0.5M $MgCl_2$) from measurements on a similar unexposed

SS304L bar under four-point bend stress. At higher Cl^- concentrations, current density (*i*) is shown to be about 2 times higher from Table 3, indicating a higher rate of dissolution. Higher *i* in higher Cl^- concentrations suggests that the bar is more susceptible to corrosion, and in the most aggressive environment, nonetheless, the effects of applied stress seem to become dominated by the Cl^- environment. However, there is a significant suppression of the steady state OCP in the tensile region compared to the compressive region in the 0.1M and 1M NaCl solutions. $MgCl_2$ solutions are generally more corrosive on stainless steels than NaCl solutions.[76] The suppressed OCP values in the tensile stress region for NaCl solutions suggests that stress effects on corrosion susceptibility are observable in less corrosive environments. OCP was not observed to be suppressed in the tensile region in the more corrosive $MgCl_2$ solutions. E_B values for the corrosion of SS304L were not observed in either solution probably because of the low S content (0.001 wt%) and the low average surface area ($8.9X10^4$ μm^2) of the SS304L working electrode in contact with electrolyte, as Bohni et al. have shown that MnS inclusions play a major role in pit initiation.[74, 86] With a low surface area and low S content (0.001 wt%), the likelihood of microcell measurements being inclusive of MnS inclusions is low, and as transpassive potential is reached, it is unlikely that inclusions are being measured. In addition, using a similar microcell setup, according to Suter et al., without MnS inclusions, applied tensile stress, varying between 60 to 80 % of the yield strength in low S content SS304 was shown to have no effect on corrosion.[21] The low likelihood of landing on MnS inclusions is the most probable reason applied stress, tensile or compressive, did not have an effect on corrosion behavior, while aggressivity from chlorides appears to be the dominant factor governing electrochemical corrosion behavior in the microcell setup used herein.

5 Implications

Under the atmospheric exposure conditions applied in this study, representative of SNF canister residual stress levels and conditions in marine location environments, electrolyte coverage and Cl^- concentration were observed to govern the pitting and corrosion susceptibility rather than the applied stress. While stress has been previously observed to affect pitting and corrosion susceptibility, through this work, it is apparent that it is not always the most deleterious factor for environmental exposures. Cl^- not only heavily affects pitting susceptibility but, as the microelectrochemical OCP data in this study implies, also overpowers any observed stress effects on current density and transpassive dissolution breakdown for the conditions measured. In aggressive salt environments, under low-humidity and high-temperature, parameters such as Cl^- concentration, electrolyte coverage and morphology along the surface, and pre-existing phase composition have a greater effect than applied stress. Therefore, these environmental parameters should also play a larger role in consideration for modeling as well as corrosion mitigation. Also, as the SS304L microstructure was not noticeably affected by the stress levels applied here, stress did not play a role in pit morphology. Rather preprocessing, i.e. cold rolling, of the SS304L metal sheet and subsequent thermal treatment is largely responsible for the induced martensite which is known to dissolve preferentially over austenite during corrosion resulting in the observed microstructural attack. Most importantly, it was found that electrolyte coverage may play a larger role than residual stress in SNF canisters. However, more studies under various conditions need to be done to fully verify this and further clarify the role of applied stress on pitting characteristics under atmospheric corrosion.

6 Conclusions:

- Pitting distribution and morphology displayed a higher dependence on the set of atmospheric exposure conditions in this study than from applied stress.
- Irregular pit morphologies observed were not observed to be influenced by the applied stress during atmospheric exposure but were formed due to interaction of the exposure environment and the underlying microstructure of the stainless steel.
- Localized microelectrochemical cell testing, where cathodic current supply is unlimited, revealed that the effects of applied stress on the electrochemical parameters related to corrosion are still obscured in the chloride environments.

ACKNOWLEDGMENTS

The authors wish to thank fellow collaborators at Sandia National Laboratories; Dr. Erin Karasz, Dr. Charles Bryan, and Alana Parey for assistance with the manuscript, Sara Dickens and Bonnie McKenzie for EBSD and SEM imaging, and Ryan Katona for assistance with MountainsMap image data processing. Sandia National Laboratories is a multimission laboratory managed and operated by National Technology & Engineering Solutions of Sandia, LLC, a wholly owned subsidiary of Honeywell International Inc., for the U.S. Department of Energy's National Nuclear Security Administration under contract DE-NA0003525. This paper describes objective technical results and analysis. Any subjective views or opinions that might be expressed in the paper do not necessarily represent the views of the U.S. Department of Energy or the United States Government.

SAND No. – ###

Figures

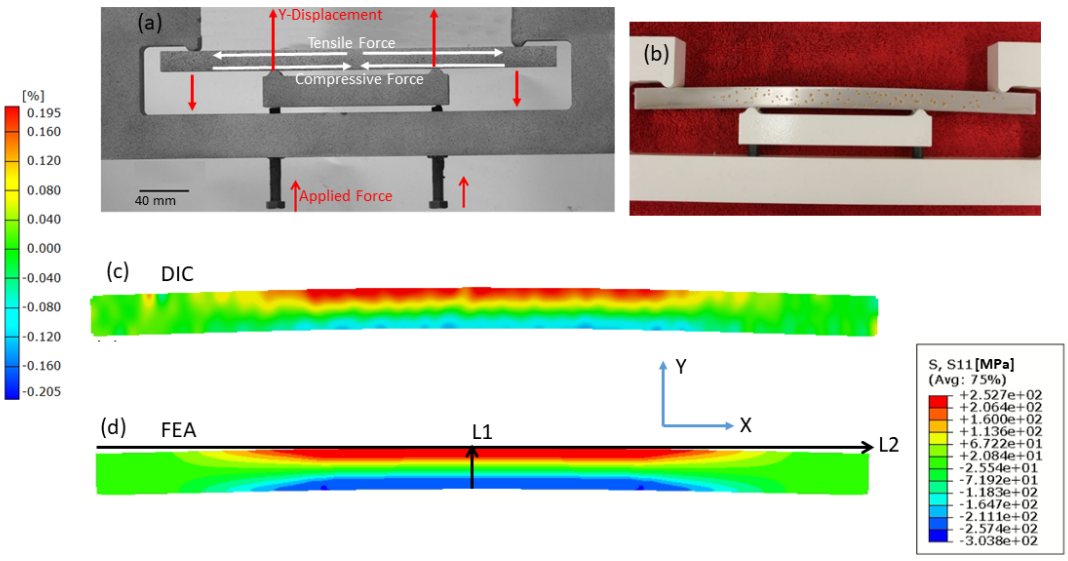

FIGURE 1. (a) Speckle pattern on the side surface of the sample for DIC analysis with specified X strain and Y displacement directions, (b) photo of the stressed SS304L bar in a four-point bend apparatus post-atmospheric exposure with corresponding (c) X-strain distribution map as measured by digital image correlation (DIC) and (d) X-stress distribution map predicted from finite element analysis (FEA). S, S11 represents stress along the XX direction.

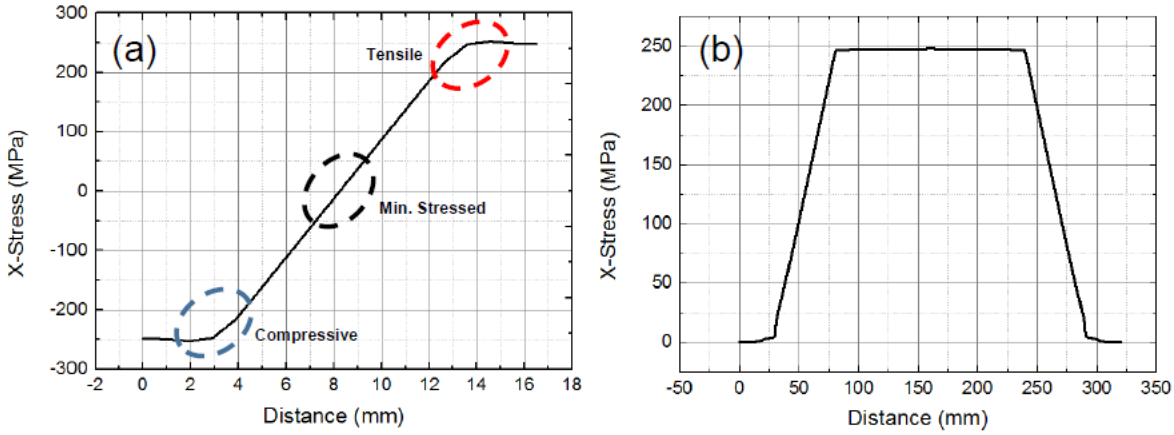

FIGURE 2. Stress distribution profiles along paths (a) L1 and (b) path L2 from the FEA in Figure 1.

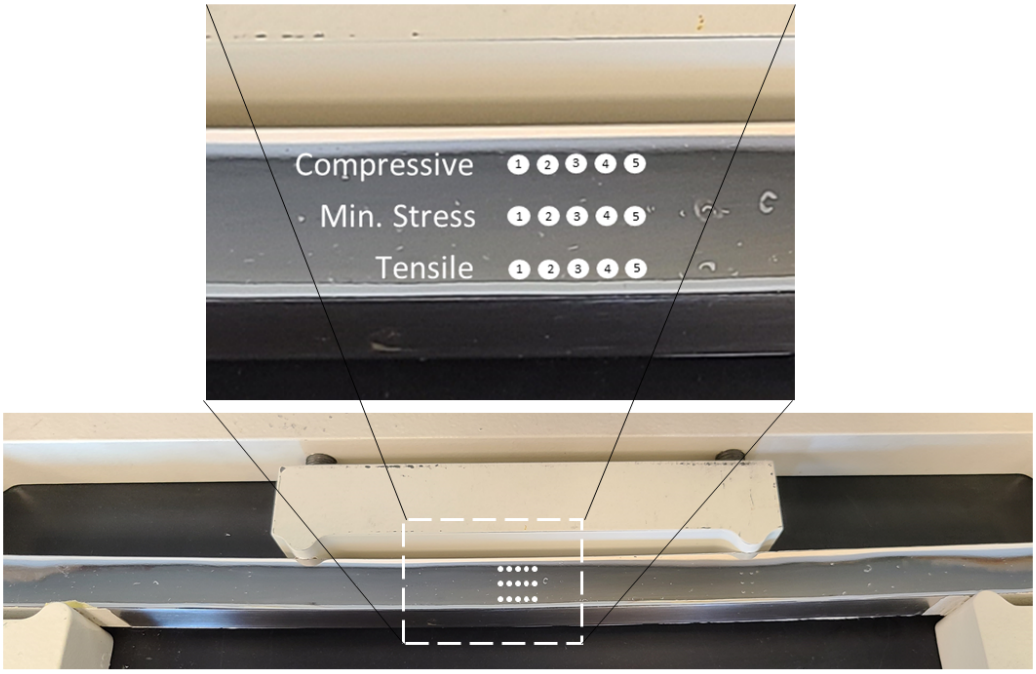

Figure 3: Image of the stressed unexposed SS304L bar, illustrating an example of the five testing areas for each maximum constant stress region in a single brine (add scale bar).

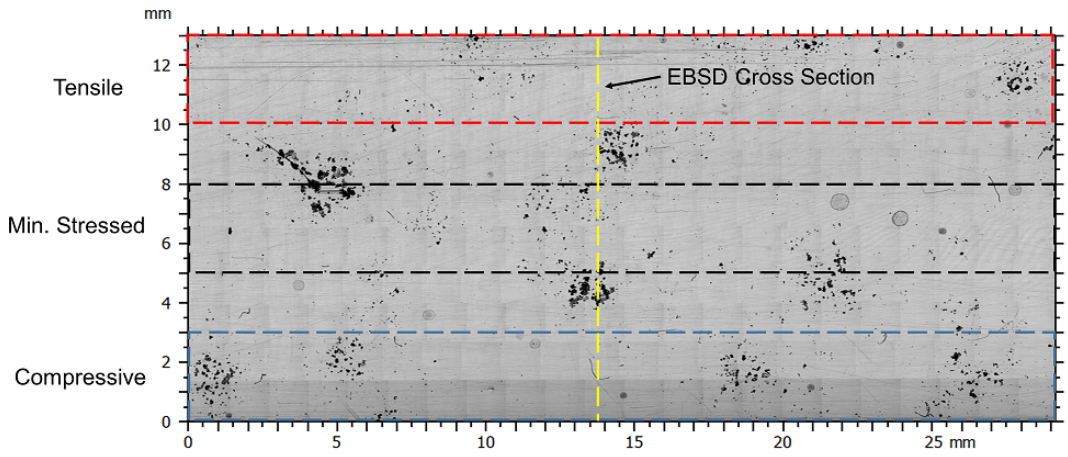

FIGURE 4. Compiled optical profilometry image for a representative scan (13mm by 29mm) of the corroded SS304L bar post atmospheric exposure and corrosion

product removal. The three respective stress regions are outlined in red (tensile), black (minimally stressed) and blue (compressive).

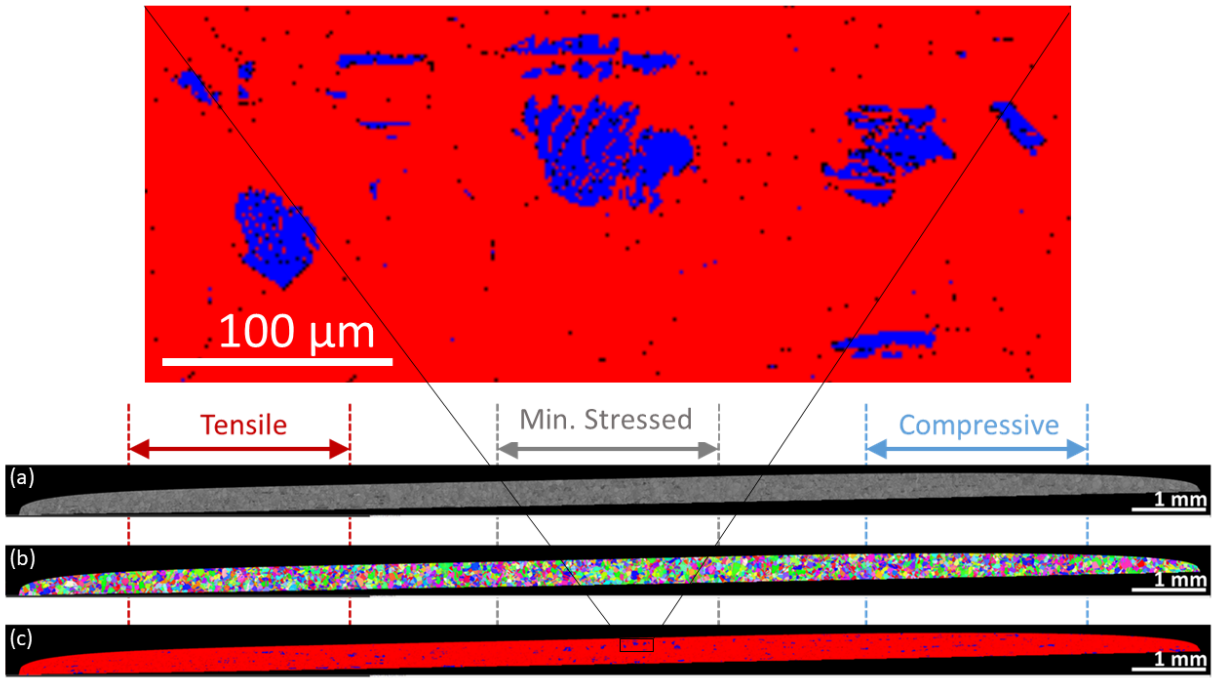

FIGURE 5. EBSD cross-section of the exposed surface of the relaxed SS304L bar with (a) band contrast, (b) IPF X map, and (c) phase contrast (where red represents FCC phases and blue represents BCC phases). Inset displays higher magnification of phase contrast map. Width of EBSD stress regions were based on the height of the outlined stress regions in Figure 4. *Note: compressive and tensile zones do not extend to edge of figure as these were cut from the data to avoid edge effects of the curved bar.

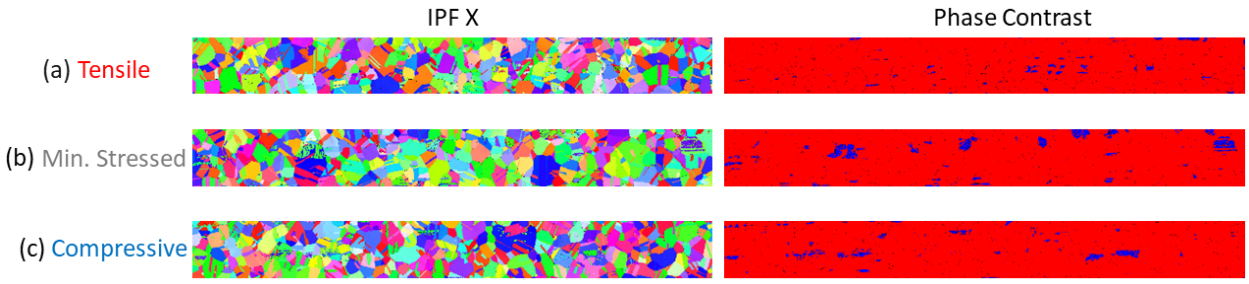

FIGURE 6. EBSD of the cross-section through the relaxed SS304L bar post-exposure for the (a) tensile, (b) minimally stressed, and (c) compressive regions for the IPF X map and phase contrast (red – FCC, blue – BCC).

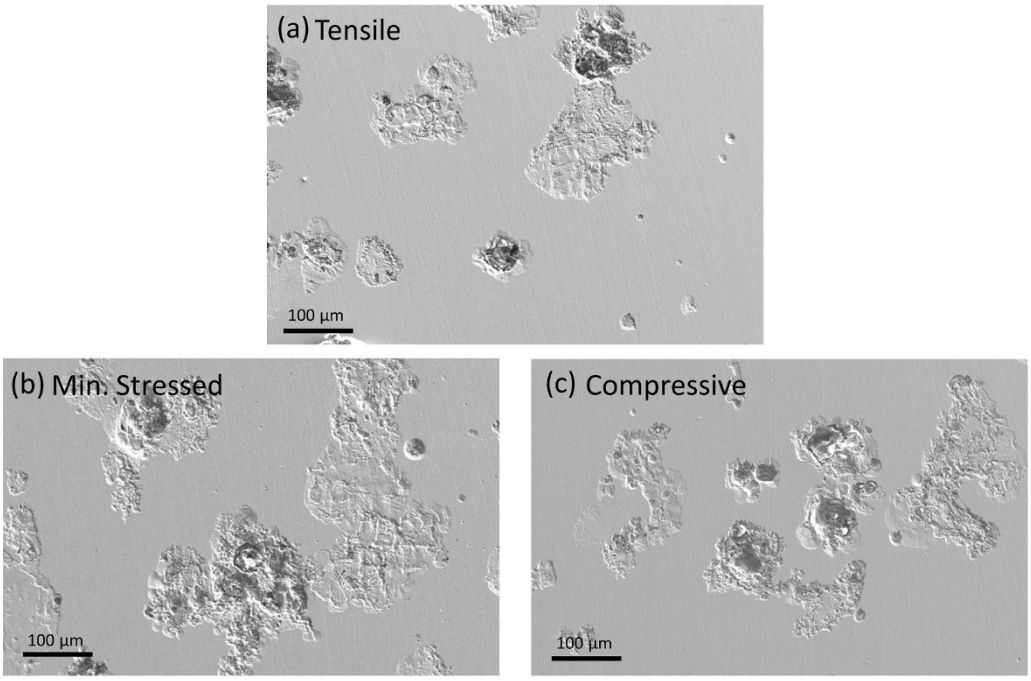

FIGURE 7. Representative SEM images of the corroded surface of the SS304L bar post atmospheric exposure and post corrosion product removal for the (a) tensile, (b) minimally stressed, and (c) compressive regions.

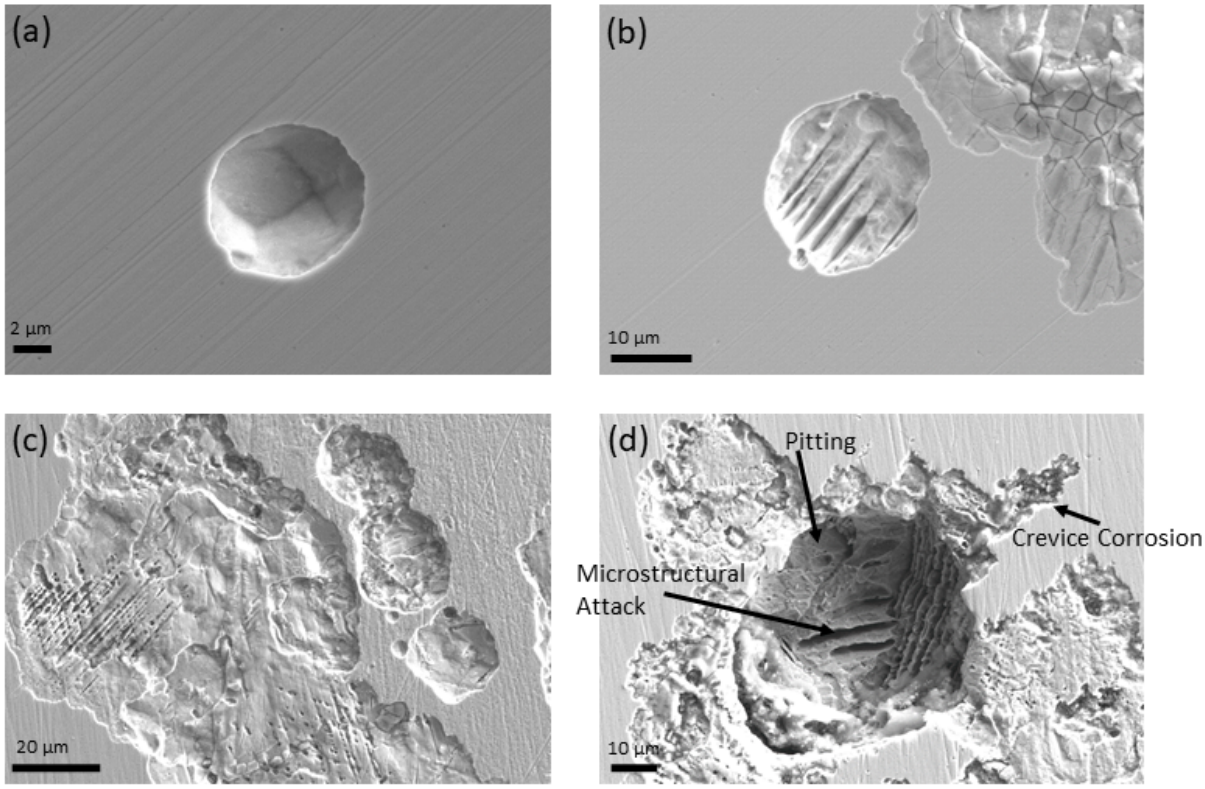

FIGURE 8. Representative SEM images of the four prominent pit morphologies observed across all regions of the SS304L bar post atmospheric exposure and post corrosion product removal: (a) hemispherical with smooth interior, (b) hemispherical with interior microstructural attack, (c) irregular shaped with shallow microstructural attack, and (d) crevice corrosion with deep microstructural attack.

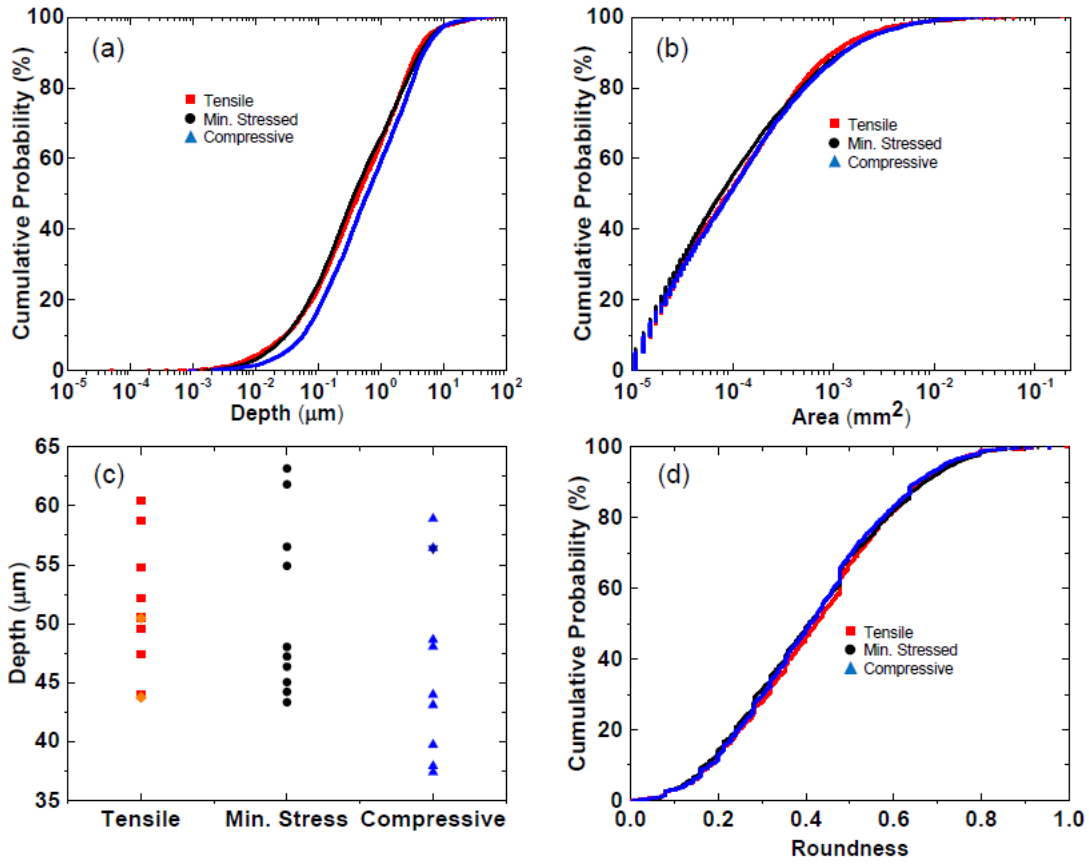

FIGURE 9. Pitting data compiled from optical profilometry measurements of the tensile, minimally stressed, and compressive regions of the SS304L bar, post exposure and corrosion product removal, for (a) pit depth, (b) pit area, (c) 10 deepest pits, and (d) pit roundness (note: curves are an assemblage of individual data points).

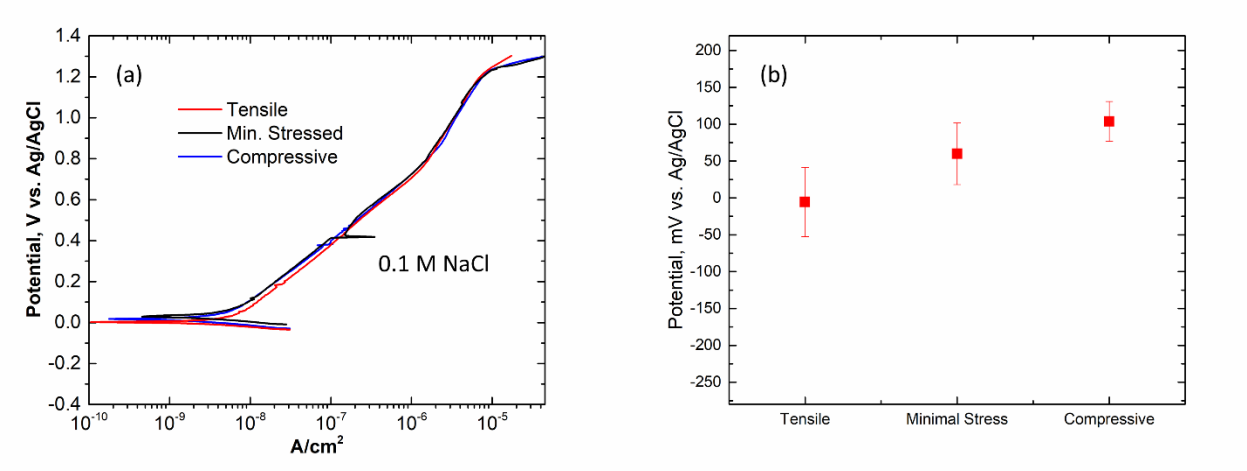

FIGURE 10. Microelectrochemical cell (a) representative potentiodynamic scans and (b) the corresponding averages of OCP for 5 scans each of the tensile, minimally stressed, and compressive regions of the stressed 304L SS bar exposed to 0.10 M NaCl (note: error bars for samples are sometimes subsumed by the sample symbols). OCP values were taken at steady state before each potentiodynamic scan.

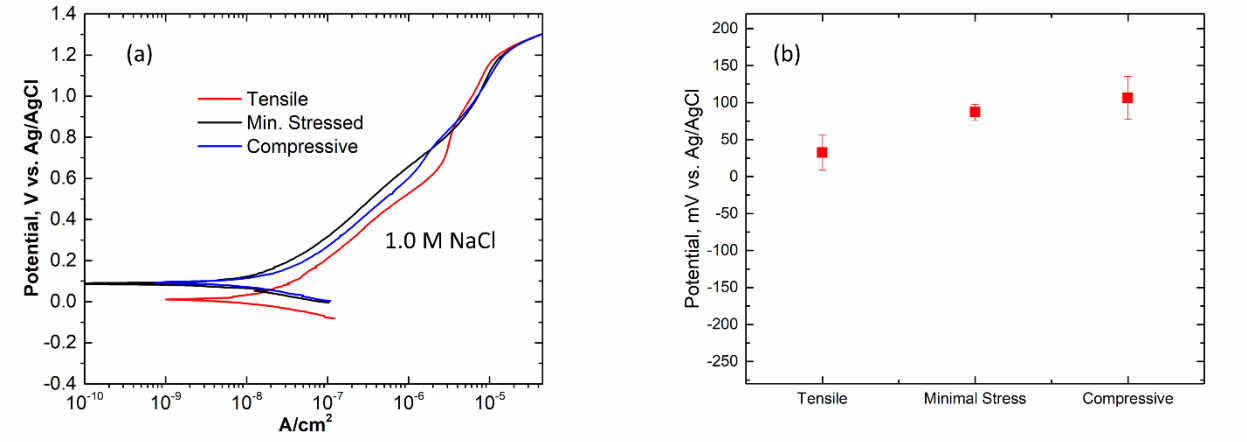

FIGURE 11. Microelectrochemical cell (a) representative potentiodynamic scans and (b) the corresponding averages of OCP for 5 scans each of the tensile, minimally stressed, and compressive regions of the stressed 304L SS bar exposed to 1 M NaCl (note: error bars for samples are sometimes subsumed by

the sample symbols). OCP values were taken at steady state before each potentiodynamic scan.

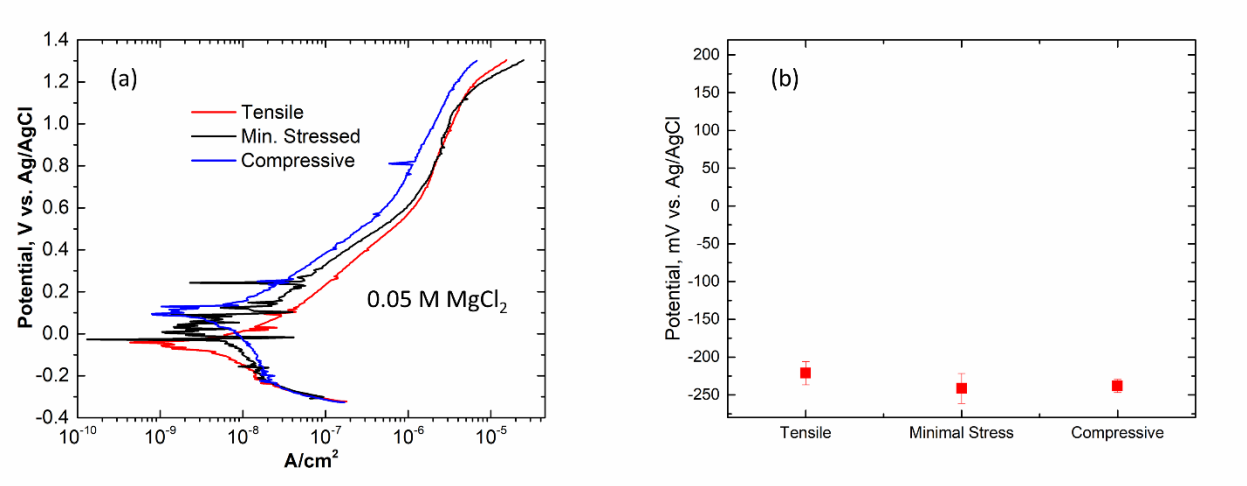

FIGURE 12. Microelectrochemical cell (a) representative potentiodynamic scans and (b) the corresponding averages of OCP for 5 scans each of the tensile, minimally stressed, and compressive regions of the stressed 304L SS bar exposed to 0.05 M $MgCl_2$ (note: error bars for samples are sometimes subsumed by the sample symbols). OCP values were taken at steady state before each potentiodynamic scan.

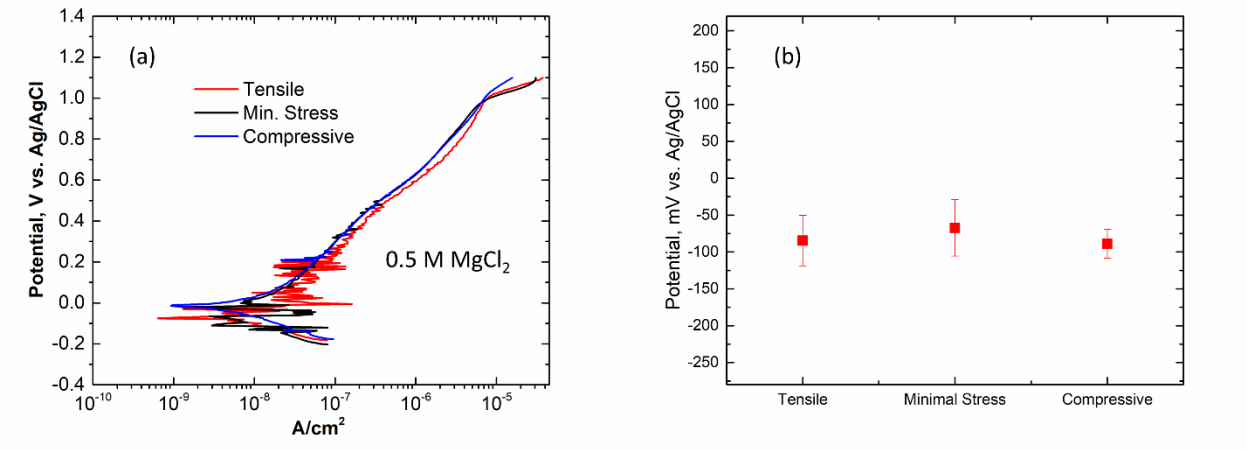

FIGURE 13. Microelectrochemical cell (a) representative potentiodynamic scans and (b) the corresponding averages of OCP for 5 scans each of the tensile, minimally stressed, and compressive regions of the stressed 304L SS bar exposed to 0.5 M $MgCl_2$ (note: error bars for samples are sometimes subsumed by the sample symbols). OCP values were taken at steady state before each potentiodynamic scan.

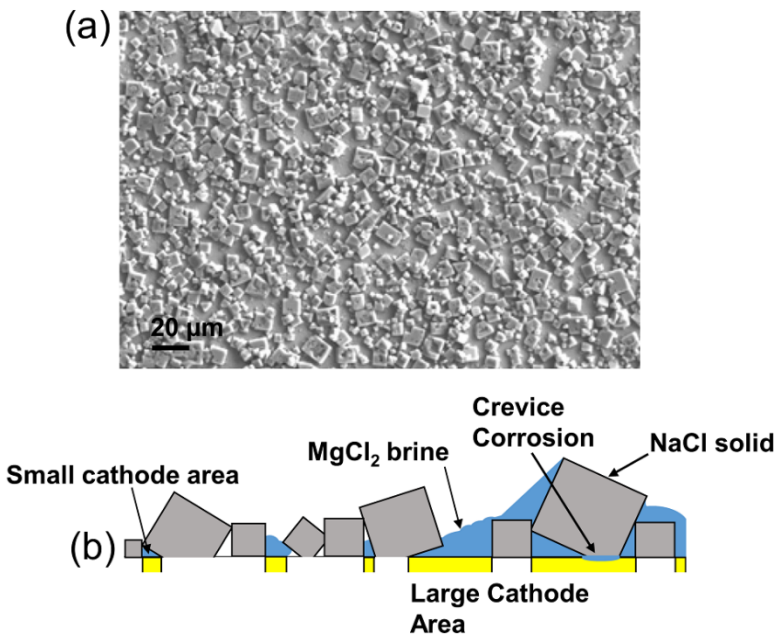

FIGURE 14. (a) SEM of the deposited salt distribution on the surface of the stressed SS304L bar and (b) schematic of salt precipitate distribution and effect on brine layer, cathodic regions, and possible crevice formation.

TABLES

Table 1. SS304L bar composition (wt %).

C	Co	Cr	Cu	Mn	Mo	N	Ni	P	S	Si	Fe
0.0216	0.198	18.3	0.392	1.83	0.286	0.0889	8.11	0.325	0.001	0.251	Bal.

Table 2. Composition of standard ASTM ASW at 25 °C and adjusted brine composition for 50 % RH and 50 °C. *35% RH Brine composition calculated using the geochemical speciation and solubility code EQ3/6,[87] and the data0.ypf.R2 Pitzer database for concentrated solutions.[88]

Component (mM/kg H_2O)	ASTM ASW 25 °C	35 % RH & 50 °C Brine*
Na^+	486	120

K^{+}	10.3	44.4
Mg^{+2}	55.3	5863
Ca^{+2}	10.58	4.04
Cl^{-}	567	11523
Br^{-}	0.86	196
F^{-}	0.07	--
SO_4^{-2}	29.16	28.9
BO_3^{-3}	0.44	101
HCO_3^{-}	2.42	76.3

Table 3. Average E_B, OCP, and *i* parameters as determined by microelectrochemical cell potentiodynamic scans for the three representative stress regions and salt concentrations.

0.1M NaCl	Transpassive E_B (mV)	OCP (mV)	*i* (μA/cm^2)
Tensile	1220±6.56	-5.64±47.1	1.86±0.427
Min. Stress	1240±7.07	59.9±41.7	1.78±0.246
Compressive	1230±12.6	104±27.0	1.66±0.116
1.0 NaCl	Transpassive E_B (mV)	OCP (mV)	*i* (μA/cm^2)
Tensile	1200±5.00	32.4±23.6	4.51±2.03
Min. Stress	1200±0	86.9±11.4	4.15±0.506
Compressive	1220±3.70	106±29.1	5.11±2.74
0.05 $MgCl_2$	Transpassive E_B (mV)	OCP (mV)	*i* (μA/cm^2)
Tensile	1150±24.3	-221±15.3	1.94±0.645
Min. Stress	1100±41.5	-241±19.8	1.51±0.395
Compressive	1190±26.0	-238±8.63	1.78±0.911
0.50 $MgCl_2$	Transpassive E_B (mV)	OCP (mV)	*i* (μA/cm^2)
Tensile	1000±2.46	-84.7±34.3	4.12±1.56
Min. Stress	994±14.9	-67.4±38.2	2.46±0.304
Compressive	1010±8.08	-88.9±19.6	2.83±0.332

References

1. Park, S. H. C.; Sato, Y. S.; Kokawa, H.; Okamoto, K.; Hirano, S.; Inagaki, M., Corrosion resistance of friction stir welded 304 stainless steel. *Scr. Mater.* **2004,** *51* (2), 101-105.
2. Weirich, T. D.; Srinivasan, J.; Taylor, J. M.; Melia, M. A.; Noe, P. J.; Bryan, C. R.; Frankel, G. S.; Locke, J. S.; Schindelholz, E. J., Humidity Effects on Pitting of Ground Stainless Steel Exposed to Sea Salt Particles. *J. Electrochem. Soc.* **2019,** *166* (11), C3477-C3487.
3. Street, S. R.; Mi, N.; Cook, A. J. M. C.; Mohammed-Ali, H. B.; Guo, L.; Rayment, T.; Davenport, A. J., Atmospheric pitting corrosion of 304L stainless steel: the role of highly concentrated chloride solutions. *Faraday Discussions* **2015,** *180* (0), 251-265.
4. Saltzstein, S. J.; Freeze, G. A.; Hanson, B.; sorenson, k. *Spent Fuel and Waste Science and Technology Storage and Transportation 5-Year R&D Plan*; United States, 2020-09-01, 2020.
5. Han, Z. Z.; He, C.; Lian, J. B.; Zhao, Y.; Chen, X., Effects of Temperature on Corrosion Behaviour of 2205 Duplex Stainless Steel in Carbon Dioxide-Containing Environments. *Int. J. Electrochem. Sci.* **2020,** *15* (5), 3627-3645.
6. Tang, Y. W.; Dai, N. W.; Wu, J.; Jiang, Y. M.; Li, J., Investigation of Influence of Surface Roughness on Pitting Corrosion of Duplex Stainless Steel 2205 using Various Electrochemical Techniques. *Int. J. Electrochem. Sci.* **2019,** *14* (7), 6790-6813.

7. Casals, N. F.; Nazarov, A.; Vucko, F.; Pettersson, R.; Thierry, D., Influence of Mechanical Stress on the Potential Distribution on a 301 LN Stainless Steel Surface. *J. Electrochem. Soc.* **2015,** *162* (9), C465-C472.
8. Långberg, M.; Örnek, C.; Evertsson, J.; Harlow, G. S.; Linpé, W.; Rullik, L.; Carlà, F.; Felici, R.; Bettini, E.; Kivisäkk, U.; Lundgren, E.; Pan, J., Redefining passivity breakdown of super duplex stainless steel by electrochemical operando synchrotron near surface X-ray analyses. *npj Materials Degradation* **2019,** *3* (1), 22.
9. Padhy, N.; Paul, R.; Mudali, U. K.; Raj, B., Morphological and compositional analysis of passive film on austenitic stainless steel in nitric acid medium. *Appl. Surf. Sci.* **2011,** *257* (11), 5088-5097.
10. Zhang, B.; Wang, J.; Wu, B.; Guo, X. W.; Wang, Y. J.; Chen, D.; Zhang, Y. C.; Du, K.; Oguzie, E. E.; Ma, X. L., Unmasking chloride attack on the passive film of metals. *Nat. Commun.* **2018,** *9*, 9.
11. Yang, Q.; Luo, J. L., Effects of hydrogen and tensile stress on the breakdown of passive films on type 304 stainless steel. *Electrochim. Acta* **2001,** *46* (6), 851-859.
12. Sedriks, A. J., *Corrosion of stainless steel, 2. edition*. John Wiley and Sons, Inc., New York, NY (United States): United States, 1996.
13. Galvele, J. R.; Torresi, R. M.; Carranza, R. M., Passivity breakdown, its relation to pitting and stress-corrosion-cracking processes. *Corrosion Sci.* **1990,** *31*, 563-571.
14. Vu, N. A.; Castel, A.; François, R., Effect of stress corrosion cracking on stress–strain response of steel wires used in prestressed concrete beams. *Corrosion Sci.* **2009,** *51* (6), 1453-1459.
15. Zhu, L. K.; Yan, Y.; Qiao, L. J.; Volinsky, A. A., Stainless steel pitting and early-stage stress corrosion cracking under ultra-low elastic load. *Corrosion Sci.* **2013,** *77*, 360-368.
16. Turnbull, A.; Wright, L.; Crocker, L., New insight into the pit-to-crack transition from finite element analysis of the stress and strain distribution around a corrosion pit. *Corrosion Sci.* **2010,** *52* (4), 1492-1498.
17. Turnbull, A.; Mingard, K.; Lord, J. D.; Roebuck, B.; Tice, D. R.; Mottershead, K. J.; Fairweather, N. D.; Bradbury, A. K., Sensitivity of stress corrosion cracking of stainless steel to surface machining and grinding procedure. *Corrosion Sci.* **2011,** *53* (10), 3398-3415.
18. Turnbull, A., Corrosion pitting and environmentally assisted small crack growth. *Proc. R. Soc. A-Math. Phys. Eng. Sci.* **2014,** *470* (2169), 19.
19. Nazarov, A.; Vivier, V.; Vucko, F.; Thierry, D., Effect of Tensile Stress on the Passivity Breakdown and Repassivation of AISI 304 Stainless Steel: A Scanning Kelvin Probe and Scanning Electrochemical Microscopy Study. *J. Electrochem. Soc.* **2019,** *166* (11), C3207-C3219.
20. Klassek, D.; Suter, T.; Schmutz, P.; Pachla, W.; Lewandowska, M.; Kurzydlowski, K. J.; von Trzebiatowski, O., The role of inclusions in the corrosion resistance of hydrostatically extruded steel products. In *HIGH PRESSURE TECHNOLOGY OF NANOMATERIALS*, Lojkowski, W.; Blizzard, J. R., Eds. 2006; Vol. 114, pp 189-195.
21. Suter, T.; Webb, E. G.; Bohni, H.; Alkire, R. C., Pit initiation on stainless steels in 1 M NaCl with and without mechanical stress. *J. Electrochem. Soc.* **2001,** *148* (5), B174-B185.
22. Lu, G. C.; Cheng, H. D.; Xu, C. C.; He, Z. H., Effect of strain and chloride concentration on pitting susceptibility for type 304 austenitic stainless steel. *Chin. J. Chem. Eng.* **2008,** *16* (2), 314-319.
23. Shimahashi, N.; Muto, I.; Sugawara, Y.; Hara, N., Effect of Applied Stress on Dissolution Morphology and Pit Initiation Behavior of MnS Inclusion in Stainless Steel. *ECS Transactions* **2014,** *58* (31), 13-22.
24. Wu, G.; Singh, P., Effect of Elastic Stresses on Pitting Behavior of Stainless Steel 304. *J. Electrochem. Soc.* **2019,** *166*, C209-C216.
25. Obata, M.; Sudo, A. In *Effect of shot peening on residual stress and stress corrosion cracking for cold worked austenitic stainless steel*, Conf Proc: ICSP-5, 1993; pp pg 257 - 264.

26. Lu, B. T.; Chen, Z. K.; Luo, J. L.; Patchett, B. M.; Xu, Z. H., Pitting and stress corrosion cracking behavior in welded austenitic stainless steel. *Electrochim. Acta* **2005,** *50* (6), 1391-1403.
27. Ghosh, S.; Rana, V. P. S.; Kain, V.; Mittal, V.; Baveja, S. K., Role of residual stresses induced by industrial fabrication on stress corrosion cracking susceptibility of austenitic stainless steel. *Mater. Des.* **2011,** *32* (7), 3823-3831.
28. Takakuwa, O.; Soyama, H., Effect of Residual Stress on the Corrosion Behavior of Austenitic Stainless Steel. *Advances in Chemical Engineering and Science* **2015,** *5* (1), 62-71.
29. Zhang, W. Q.; Fang, K. W.; Hu, Y. J.; Wang, S. Y.; Wang, X. L., Effect of machining-induced surface residual stress on initiation of stress corrosion cracking in 316 austenitic stainless steel. *Corrosion Sci.* **2016,** *108*, 173-184.
30. Almuaili, F. A.; McDonald, S. A.; Withers, P. J.; Cook, A. B.; Engelberg, D. L., Strain-induced reactivation of corrosion pits in austenitic stainless steel. *Corrosion Sci.* **2017,** *125*, 12-19.
31. Lieberzeit, J.; Prosek, T.; Jarvis, A.; Kiener, L., Atmospheric Stress Corrosion Cracking of Stainless Steel Rock Climbing Anchors, Part 1. *Corrosion* **2019,** *75* (10), 1255-1271.
32. Prosek, T.; Lieberzeit, J.; Jarvis, A.; Kiener, L., Atmospheric Stress Corrosion Cracking of Stainless Steel Rock Climbing Anchors, Part 2: Laboratory Experiments. *Corrosion* **2019,** *75* (11), 1371-1382.
33. Ornek, C., Stress Corrosion Cracking and Hydrogen Embrittlement of Type 316L Austenitic Stainless Steel Beneath MgCl2 and MgCl2: FeCl3 Droplets. *Corrosion* **2019,** *75* (6), 657-667.
34. Deng, D.; Murakawa, H.; Lang, W., Numerical and experimental investigations on welding residual stress in multi-pass butt-welded austenitic stainless steel pipe. *Comput. Mater. Sci.* **2008,** *42* (2), 234-244.
35. Schindelholz, E. J.; Bryan, C. R.; Alexander, C. L. *FY17 Status Report: Research on Stress Corrosion Cracking of SNF Interim Storage Canisters*; United States, 2017-09-01, 2017.
36. Bryan, C. R.; Schindelholz, E. J. *FY18 Status Report: SNL Research into Stress Corrosion Cracking of SNF Interim Storage Canisters*; United States, 2018-11-01, 2018.
37. Teague, M. C.; Saltzstein, S. J.; Hanson, B.; Sorenson, K. B.; Freeze, G. A. *Gap Analysis to Guide DOE R&D in Supporting Extended Storage and Transportation of Spent Nuclear Fuel: An FY2019 Assessment (Final Report)*; United States, 2019-12-23, 2019.
38. Cook, A.; Duff, J.; Stevens, N.; Lyon, S.; Sherry, A.; Marrow, T. J., Preliminary Evaluation of Digital Image Correlation for In-situ Observation of Low Temperature Atmospheric-Induced Chloride Stress Corrosion Cracking in Austenitic Stainless Steels. In *Corrosion*, Hansen, D. C.; Missert, N.; Inman, M.; Garfias, L. F.; Lillard, R. S., Eds. Electrochemical Soc Inc: Pennington, 2010; Vol. 25, pp 119-132.
39. Cook, A. B.; Lyon, S. B.; Stevens, N. P. C.; Gunther, M.; McFiggans, G.; Newman, R. C.; Engelberg, D. L., Assessing the risk of under-deposit chloride-induced stress corrosion cracking in austenitic stainless steel nuclear waste containers. *Corros. Eng. Sci. Technol.* **2014,** *49* (6), 529-534.
40. Cook, A.; Padovani, C.; Davenport, A. J., Effect of Nitrate and Sulfate on Atmospheric Corrosion of 304L and 316L Stainless Steels. *J. Electrochem. Soc.* **2017,** *164* (4), C148-C163.
41. Engelberg, D. L.; Ornek, C., Probing propensity of grade 2205 duplex stainless steel towards atmospheric chloride-induced stress corrosion cracking. *Corros. Eng. Sci. Technol.* **2014,** *49* (6), 535-539.
42. Newman, R. C., 2001 W.R. Whitney Award Lecture: Understanding the corrosion of stainless steel. *Corrosion* **2001,** *57* (12), 1030-1041.
43. Ornek, C.; Engelberg, D. L., Toward Understanding the Effects of Strain and Chloride Deposition Density on Atmospheric Chloride-Induced Stress Corrosion Cracking of Type 304 Austenitic Stainless Steel Under MgCl2 and FeCl3:MgCl2 Droplets. *Corrosion* **2019,** *75* (2), 167-182.
44. Ornek, C.; Engelberg, D. L., Towards understanding the effect of deformation mode on stress corrosion cracking susceptibility of grade 2205 duplex stainless steel. *Mater. Sci. Eng. A-Struct. Mater. Prop. Microstruct. Process.* **2016,** *666*, 269-279.

45. Ornek, C.; Zhong, X. L.; Engelberg, D. L., Low-Temperature Environmentally Assisted Cracking of Grade 2205 Duplex Stainless Steel Beneath a MgCl2:FeCl3 Salt Droplet. *Corrosion* **2016,** *72* (3), 384-399.
46. Ornek, C.; Leonard, F.; McDonald, S. A.; Prajapati, A.; Withers, P. J.; Engelberg, D. L., Time-dependent in situ measurement of atmospheric corrosion rates of duplex stainless steel wires. *Npj Materials Degradation* **2018,** *2* (1), 15.
47. Scatigno, G. G.; Dong, P.; Ryan, M. P.; Wenman, M. R., The effect of salt loading on chloride-induced stress corrosion cracking of 304L austenitic stainless steel under atmospheric conditions. *Materialia* **2019,** *8*, 11.
48. Spencer, D. T.; Edwards, M. R.; Wenman, M. R.; Tsitsios, C.; Scatigno, G. G.; Chard-Tuckey, P. R., The initiation and propagation of chloride-induced transgranular stress-corrosion cracking (TGSCC) of 304L austenitic stainless steel under atmospheric conditions. *Corrosion Sci.* **2014,** *88*, 76-88.
49. Kondo, Y., Prediction of Fatigue Crack Initiation Life Based on Pit Growth. *Corrosion* **1989,** *45* (1), 7-11.
50. Mai, W.; Soghrati, S.; Buchheit, R. G., A phase field model for simulating the pitting corrosion. *Corrosion Sci.* **2016,** *110*, 157-166.
51. Mai, W.; Soghrati, S., A phase field model for simulating the stress corrosion cracking initiated from pits. *Corrosion Sci.* **2017,** *125*, 87-98.
52. Mai, W.; Soghrati, S., New phase field model for simulating galvanic and pitting corrosion processes. *Electrochim. Acta* **2018,** *260*, 290-304.
53. Rudomilova, D.; Prosek, T.; Strom, M., Hydrogen Entry into Steel Under Corrosion Products. *Corrosion* **2021,** *77* (4), 427-432.
54. McMurtrey, M. D.; Mills, D. E.; Burns, J. T., The effect of pit size and density on the fatigue behaviour of a pre-corroded martensitic stainless steel. *Fatigue & Fracture of Engineering Materials & Structures* **2019,** *42* (1), 3-18.
55. Mohammed-Ali, H. B.; Street, S. R.; Attallah, M. M.; Davenport, A. J., Effect of Microstructure on the Morphology of Atmospheric Corrosion Pits in Type 304L Stainless Steel. *Corrosion* **2018,** *74* (12), 1373-1384.
56. Cerit, M.; Genel, K.; Eksi, S., Numerical investigation on stress concentration of corrosion pit. *Engineering Failure Analysis* **2009,** *16* (7), 2467-2472.
57. Co, N. E. C.; Burns, J. T., Galvanic Corrosion-Induced Fatigue Crack Initiation and Propagation Behavior in AA7050-T7451. *Corrosion* **2016,** *72* (10), 1215-1219.
58. Tokuda, S.; Muto, I.; Sugawara, Y.; Hara, N., Pit initiation on sensitized Type 304 stainless steel under applied stress: Correlation of stress, Cr-depletion, and inclusion dissolution. *Corrosion Sci.* **2020,** *167*, 12.
59. Tokuda, S.; Muto, I.; Sugawara, Y.; Hara, N., The role of applied stress in the anodic dissolution of sulfide inclusions and pit initiation of stainless steels. *Corrosion Sci.* **2021,** *183*, 109312.
60. Guo, S.; Wang, H.; Han, E.-H., Computational Evaluation of the Influence of Various Uniaxial Load Levels on Pit Growth of Stainless Steel under Mechanoelectrochemical Interactions. *J. Electrochem. Soc.* **2018,** *165* (9), C515-C523.
61. Greenspan, L., Humidity fixed points of binary saturated aqueous solutions. *Journal of Research of the National Bureau of Standards Section A: Physics and Chemistry* **1977**, 89-96.
62. Shayer, Z. *Innovative Approach to SCC Inspection and Evaluation of Canister in Dry Storage*; United States, 2019-10-30, 2019.
63. D6272-17, A., Standard Test Method for Flexural Properties of Unreinforced and Reinforced Plastics and Electrical Insulating Materials by Four-Point Bending. *West Conshohocken, PA* **2020**.
64. G39-99, A., Standard Practice for Preparation and Use of Bent-Beam Stress-Corrosion Test Specimens. *West Conshohocken, PA* **2021**.

65. D1141-98, A., Standard Practice for the Preparation of Substitute Ocean Water. *West Conshohocken, PA* **2013**.
66. Wolery, T. J. *EQ3/6, a software package for geochemical modeling of aqueous systems: Package overview and installation guide (Version 7.0)*; United States, 1992-09-14, 1992.
67. SNL, In-Drift Precipitates/Salts Model. *ANL-EBS-MD-000045 REV 03 (Albuquerque, NM, Sandia National Laboratories, 2007): p.358* **2007**.
68. G1-03, A., Standard Practice for Preparing, Cleaning, and Evaluating Corrosion Test Specimens. *West Conshohocken, PA* **2017**.
69. MountainsMap-, *Reference Manual*. Digital Surf: 2016.
70. G16-13, A., Standard Guide for Applying Statistics to Analysis of Corrosion Data. *West Conshohocken, PA* **2019**.
71. Helsel, D. R.; Hirsch, R. M. *Statistical methods in water resources*; 04-A3; Reston, VA, 2002.
72. Hassel, A. W.; Fushimi, K.; Seo, M., An agar-based silver|silver chloride reference electrode for use in micro-electrochemistry. *Electrochemistry Communications* **1999,** *1* (5), 180-183.
73. López, D. M.; Alonso Falleiros, N.; Tschiptschin, A. P., Use of Electrochemical Tests for Assessment of the Effect of Erosive Particle Size on the Erosion-Corrosion Behaviour of AISI 304L Austenitic Stainless Steel. *Materials Research* **2016,** *19*, 451-458.
74. Okeniyi, J. O.; Loto, C. A.; Popoola, A. P. I., Corrosion inhibition performance of Rhizophora mangle L bark-extract on concrete steel-reinforcement in industrial/microbial simulating-environment. *Int. J. Electrochem. Sci.* **2014,** *9* (8), 4205-4216.
75. Fattah-Alhosseini, A.; Attarzadeh, N., The Mechanism of Transpassive Dissolution of AISI 321 Stainless Steel in Sulphuric Acid Solution. *International Journal of Electrochemistry* **2011,** *2011*, 521384.
76. Böhni, H.; Suter, T.; Schreyer, A., Micro- and nanotechniques to study localized corrosion. *Electrochim. Acta* **1995,** *40* (10), 1361-1368.
77. Chen, Z. Y.; Kelly, R. G., Computational Modeling of Bounding Conditions for Pit Size on Stainless Steel in Atmospheric Environments. *J Electrochem Soc* **2010,** *157* (2), C69-C78.
78. Katona, R. M.; Carpenter, J. C.; Knight, A. W.; Bryan, C. R.; Schaller, R. F.; Kelly, R. G.; Schindelholz, E. J., Importance of the hydrogen evolution reaction in magnesium chloride solutions on stainless steel. *Corrosion Sci.* **2020,** *177*, 108935.
79. Katona, R. M.; Knight, A. W.; Schindelholz, E. J.; Bryan, C. R.; Schaller, R. F.; Kelly, R. G., Quantitative assessment of environmental phenomena on maximum pit size predictions in marine environments. *Electrochim. Acta* **2021,** *370*, 137696.
80. Guo, L. Y.; Mi, N.; Mohammed-Ali, H.; Ghahari, M.; Du Plessis, A.; Cook, A.; Street, S.; Reinhard, C.; Atwood, R. C.; Rayment, T.; Davenport, A. J., Effect of Mixed Salts on Atmospheric Corrosion of 304 Stainless Steel. *J. Electrochem. Soc.* **2019,** *166* (11), C3010-C3014.
81. Monrrabal, G.; Bautista, A.; Guzman, S.; Gutierrez, C.; Velasco, F., Influence of the cold working induced martensite on the electrochemical behavior of AISI 304 stainless steel surfaces. *Journal of Materials Research and Technology* **2019,** *8* (1), 1335-1346.
82. Pardal, J. M.; da Silva, M. R.; Bastos, I. N.; de Macedo, M. C. S.; Tavares, S. S. M., Influence of tempering treatment on microstructure and pitting corrosion resistance of a new super ferritic-martensitic-austenitic stainless steels with 17%Cr. *Corros. Eng. Sci. Technol.* **2016,** *51* (5), 337-341.
83. Rafiee, E.; Farzam, M.; Golozar, M. A.; Ashrafi, A., An Investigation on Dislocation Density in Cold-Rolled Copper Using Electrochemical Impedance Spectroscopy. *ISRN Corrosion* **2013,** *2013*, 921825.
84. de Abreu, H. F. G.; Gomes da Silva, M. J.; Maia do Nascimento, A.; Freitas, F. N. C., Stress induced martensite transformation texture in AISI 304 austenitic stainless steel. *Materials Science and Technology* **2011,** *27* (11), 1627-1631.

85. Qin, Z.; Xia, Y., Role of strain-induced martensitic phase transformation in mechanical response of 304L steel at different strain-rates and temperatures. *Journal of Materials Processing Technology* **2020,** *280*, 116613.
86. Shi, X.; Zhou, G.; Muthumani, A., Corrosion of metals exposed to 25% magnesium chloride solution and tensile stress: Field and laboratory studies. *Case Studies in Construction Materials* **2017,** *7*, 1-14.
87. Navaï, F., Effects of tensile and compressive stresses on the passive layers formed on a type 302 stainless steel in a normal sulphuric acid bath. *Journal of Materials Science* **1995,** *30* (5), 1166-1172.
88. Böhni, H.; Suter, T.; Assi, F., Micro-electrochemical techniques for studies of localized processes on metal surfaces in the nanometer range. *Surface and Coatings Technology* **2000,** *130* (1), 80-86.